Available online at www.sciencedirect.com
SCIENCE DIRECT®
Journal of Nuclear Materials 348 (2006) 229–242
journal of nuclear materials
www.elsevier.com/locate/jnucmat

Fission product release in high-burn-up UO_2 oxidized to U_3O_8

J.Y. Colle [a], J.-P. Hiernaut [a], D. Papaioannou [a], C. Ronchi [a,*], A. Sasahara [b]

[a] European Commission, Joint Research Centre, European Institute for Transuranium Elements, P.O. Box 2340, 76125 Karlsruhe, Germany
[b] Nuclear Energy Systems Department, Komae Research Laboratory, Central Research Institute of Electric Power Industry, 2-11-1 Iwado Kita, Komae-shi, Tokyo 201, Japan

Received 20 April 2005; accepted 27 September 2005

Abstract

Results of oxidation experiments on high-burn-up UO_2 are presented where fission-product vaporisation and release rates have been measured by on-line mass spectrometry as a function of time/temperature during thermal annealing treatments in a Knudsen cell under controlled oxygen atmosphere. Fractional release curves of fission gas and other less volatile fission products in the temperature range 800–2000 K were obtained from BWR fuel samples of 65 GWd t^{-1} burn-up and oxidized to U_3O_8 at low temperature. The diffusion enthalpy of gaseous fission products and helium in different structures of U_3O_8 was determined.

1. Introduction

Though the equilibrium thermodynamic properties of uranium dioxide are well established, the rare-gas atomic mobility in the fcc lattice of UO_{2+x} is still matter of debate. This is principally due to the variety of possible lattice defect configurations influencing the atomic jumps, which are in turn governed by the chemical activity of oxygen and associated changes of the local uranium valence. The problem increases in complexity as more uranium atoms attain higher oxidation states.

The thermochemical stability of uranium dioxide continuously decreases if more oxygen is added in the UO_{2+x} cubic solid solution up to the high O/U ratios at which the less compacted orthorhombic structure of U_3O_{8-x} is formed, displaying a markedly different physical character. Though the thermodynamic data of the stoichiometric uranium oxides have been consolidated in comprehensive databases (see, e.g., the analysis made by Gurvich et al. [1]), the phase diagram of the U–O system still presents some unknown aspects and unresolved problems. A view of the present state of the art is given by recent exhaustive review articles [2–4]. If one considers the available data and their uncertainty, for moderately high temperatures (up to 1500 K), the thermodynamic properties in the phase diagram domain between U_4O_9 and U_3O_8 are reasonably well known; whilst data regarding the system U_3O_8–UO_3 are not fully in agreement. Conversely, at higher temperatures, the entire U–O phase diagram for $O/U > 2$ presents considerable inconsistencies and lacunae. For instance, recent

* Corresponding author. Tel.: +49 7247 951 402; fax: +49 7247 951 99402.
E-mail address: ronchi@itu.fzk.de (C. Ronchi).

0022-3115/$ - see front matter © 2005 Elsevier B.V. All rights reserved.
doi:10.1016/j.jnucmat.2005.09.024

experiments [5] have shown that new accurate solidus/liquidus data of the cubic solid solution UO_{2+x} differ from those obtained in the past with conventional melting techniques, and that the extra-oxygen effect on the free energy of the UO_{2+x} solid solution is stronger than previously assumed.

For the higher oxides, despite the extensive work performed and the copious literature on the subject, the properties are much more uncertain. Several experiments, conducted under different oxidation conditions, provide evidence for chemical dissociation of the orthorhombic or hexagonal U_3O_8 with a measured decomposition temperature – i.e., the temperature at which formation of a cubic phase starts – ranging from 1300 K to 1700 K. Endeavours to measure the triple point of U_3O_8 failed so far.

A characteristic high-temperature feature of uranium oxide with $O/U > 2$ is the predominance of $UO_3(g)$ among the uranium-bearing components of the equilibrium vapour, as well as a much higher oxygen partial pressure. This is due to intricate non-congruent surface vaporisation mechanisms where oxygen diffusion and activation of hexa-valent uranium bonding play a key role. As a consequence, maintaining at high temperatures a constant O/U composition may require a control of the oxygen partial pressure at levels which are hardly practicable in a number of laboratory experiments; and when this is possible, sublimation rate and oxidation kinetics are so fast that oxygen pressure control becomes anyway very difficult. In the reported work, two different approaches were pursued, described in some more detail in a previous paper [6]: in a first type of experiments, the composition of the oxide was kept as far as possible constant in the explored temperature range, in the second one, the oxygen partial pressure was fixed, and the changes in composition with temperature were analysed. This made it possible to establish a temperature range where fission-gas diffusion measurements could be carried out under conditions close to thermochemical equilibrium.

2. Experimental setup

The experiments were carried out in a Knudsen-effusion setup. Samples of approximately 10 mg weight are contained in a small sample holder made of platinum that is placed in an alumina Knudsen cell (10 mm ∅ and 5 mm *h*) with an aperture variable between 0.3 and 1 mm. The cell is heated in a vacuum by a tungsten coil surrounded by seven thermal shields ensuring temperature homogeneity in the cell. From thermocouple measurements, at 1900 K the dimensions of the homogeneous (±5 K) zone in the furnace are 30 mm ∅ and 60 mm *h*; above 700 K the effective thermal inertia of the furnace is small, enabling steady state temperature changes to be applied within a few minutes. The bottom of the cell has a cylindrical aperture into which an alumina capillary (1 mm ∅) is inserted to enable a gas inflow in an antechamber 'labyrinth' where the gas is heated before entering the cell. The gas is introduced from an external reservoir at a controlled pre-fixed pressure, and the relationship between the oxygen pressure in the reservoir and that in the cell is obtained from laminar flow equations. In order to provide a prompt response, the volume of the reservoir is kept as small as possible and its pressure is regulated by a gas inlet, electronically steered micro valve. Since in our case oxygen represents by far the major vapour component in the Knudsen cell, a given constant pressure can be established in the cell by using as a feedback to the inlet valve either the mass spectrometer signal of oxygen or the vacuum gauge current. The molecular beam effusing from the cell aperture is directed through a sequence of apertures in the thermal shields to the upper, water-cooled, cover plate of the vessel where through a small hole of 5 mm ∅ the beam is collimated into the ion source of a quadrupole mass spectrometer (MS) placed in the otherwise separated upper chamber. The ion source is surrounded by a large liquid-nitrogen trap, which, in conjunction with use of oil-free turbo-molecular and rotary pumps, does effectively remove from the rest gas most disturbing hydrocarbon components. The attainable pressure in the MS chamber is of the order of 10^{-10} Torr, and increases to the MS operation limit of 10^{-5} Torr as a gas inflow is allowed in the underneath furnace vessel. This is evacuated by an independent pumping system consisting of two sequential turbo molecular pumps connected to a Leybold 'Dryvac' oil-free primary vacuum pump.

In practice, the operating differential pumping system makes it possible to maintain in the Knudsen-cell oxygen pressures up to of the order of 1000 Pa, however, limits for Knudsen-effusion conditions were more restrictive than those necessary to perform gas release measurements. Calibration of the gas inflow producing the wished pressure in the cell proved to be possible with suitable

standards, by checking the stability of the steady-state sublimation rate of pre-fixed UO_{2+x} compounds after manually establishing the O/O_2 equilibrium partial pressure expected at the given temperature. The performance of the experimental setup is described in more detail in Ref. [6].

3. Samples

A Boiling Water Reactor fuel rod irradiated up to 65 GWd t^{-1} burn-up was selected for this investigation. Samples were taken from pellets, where the in-pile temperature was low enough to maintain all fission products homogeneously dispersed or frozen in the lattice. In particular, fission gas is present at the end of irradiation in largely hyper-saturated concentrations of the order of 15 000 at. ppm. For these samples, the experiment shows that during thermal annealing, in a vacuum and over times of a few hours, fission-gas release and volatile fission products like caesium starts at ≈1000 K, and is effectively complete below 2000 K.

Under oxidation conditions, diffusion processes become faster; nonetheless, if the oxidation temperature does not exceed 750 K, most fission products are entirely retained in the matrix. Even the fission gas precipitated in-pile in grain boundary pores did not escape in a significant amount during low-temperature oxidation. This was attested by monitoring ^{85}Kr release during oxidation: only 2–5% of the gas initially present in the fuel was released. In view of that, samples oxidized at these low temperatures are in a suitable state to investigate fission-product diffusion by subsequent thermal treatments. Yet, the essential prerequisite is to bring about environmental conditions apt to sufficiently maintain the preset sample stoichiometry.

3.1. Reference compounds

Definition of a reference oxide phase corresponding to a highly oxidized state of fission-product doped UO_2 is not straightforward, all the more since U_3O_8 presents a pronounced polymorphism in its crystal forms (see, e.g., [7]). The first question to answer concerns the type of structure expected from oxidation of irradiated UO_2 containing a total concentration of fission products of the order of magnitude of 10 at.%. The correspondence between the oxidation behaviour of the irradiated fuel and that of pure UO_2 was, therefore, investigated under similar conditions.

If one just considers the three more common forms of U_3O_8 – α (face-centred orthorhombic, with two types of U-positions), α′ (hexagonal high-temperature modification of α, with one type of U-positions) and β (trigonal, of lower density) – different phase transitions can occur during thermal annealing, even if the oxide composition is kept constant, depending not only on temperature, but also on the applied temperature programme.

Our reference samples were prepared from a U_3O_8 sintered powder (crystal grains of a few micrometers size) oxidized at 700 K. XRD analysis indicates the presence of a single phase with an orthorhombic structure of space group *C*222, with parameters $\{a,b,c\} = \{0.6715, 1.1959, 0.4146\}$ nm, which closely corresponds to the α-phase reported in the literature [8].

The powder was then cold-pressed in the form of pellets and sintered at 1400 K in oxygen at 1 bar. In the product, an almost complete phase change was detected from the α- to the β-phase with space group *Cmcm*, with parameters $\{a,b,c\} = \{0.7069, 1.1445, 0.8302\}$ nm. This is in agreement with U_3O_8 structures found under similar conditions [9]. With respect to that of the starting powder, the crystal density decreases after sintering from approximately 8.39 to 8.35 g cm^{-3}. In the two ideal structures, the uranium sub-lattice maintains the same symmetry positions, whilst the oxygen sub-lattice exhibits a markedly different coordination, surrounding two U-atoms with a pentagonal dipyramid and three U-atoms with a deformed octahedron. In fact, for both the α- and β-phase the experimental XRD peak intensities could only be approximately reproduced; indexing was also incomplete. Fig. 1(a) and (b) show the respective XRD spectra of the orthorhombic U_3O_8 with space group *C*222 and *Cmcm*, compared with the theoretical predictions calculated from the atomic positions reported in the literature. One can see that the deviations of some of the line intensities are appreciable; however, the correspondence of the peak positions is sufficient to ensure correctness of the deduced unit cell. Further attempts to obtain a better fitting were beyond the scope of our investigation.

The distinctive attribute of these structures is that UO layers are formed in the basal plane between which the remnant oxygen is distributed in chains along the *z*-direction (Fig. 2). This lattice configuration can easily adapt to fit in considerable oxygen stoichiometric deviations as well as foreign atoms that can be accommodated in the large interstitial

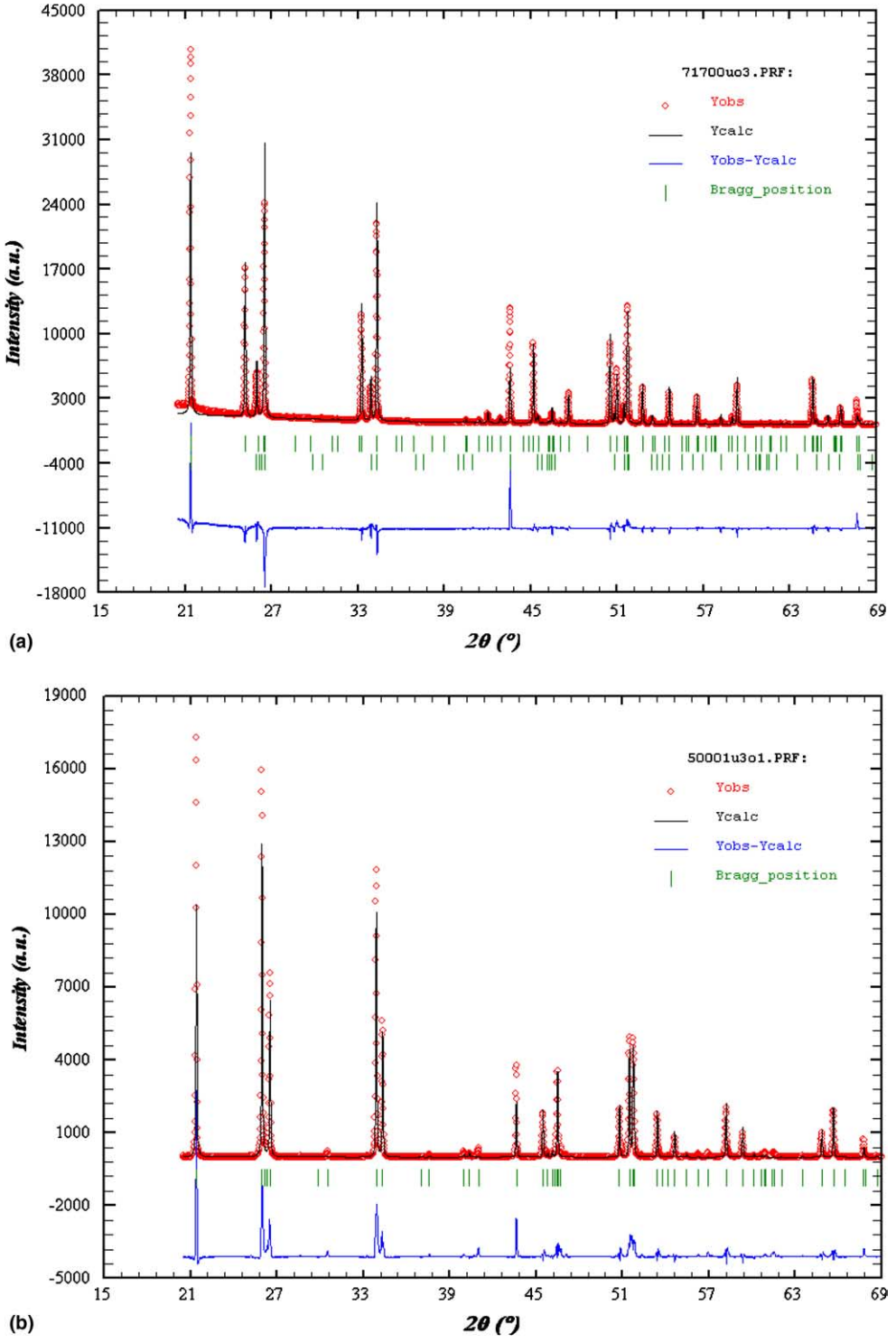

Fig. 1. XRD spectra of U_3O_8: (a) crystal phase with space group *C*222, (b) crystal phase with space group *Cmcm*.

voids, as shown in Fig. 2 for xenon. Furthermore, it can be readily seen that creation of oxygen Frenkel pairs of different crystallographic configurations in such a structure is possible for adjacent uranium

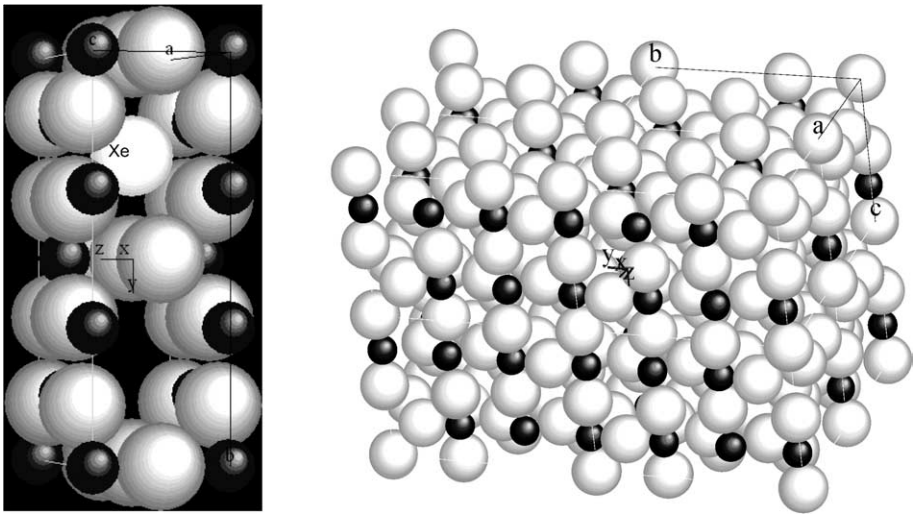

Fig. 2. Lattice model of the orthorhombic lattice of α-U_3O_8. In the enlarged cell the probable position of a xenon atom (light grey sphere) in an interstitial void is indicated.

atoms can adapt by changing the oxidation state from U^{4+} to U^{6+}. It is, however, worth remarking that, contrary to the cubic UO_{2+x}, the orthorhombic lattice is unable to sustain large strains produced by cationic defects, and lattice disruption is observed when, for instance, U_3O_8 is submitted to radiation damage.

3.2. Oxidation of irradiated samples

The structure of the oxidized irradiated samples is affected by the presence of fission products. Furthermore, U_3O_8 at temperatures below 400 K is almost completely destroyed by radiation damage already at doses of 10^{17}–10^{18} fissions cm^{-3} [10,11]. Since thermal healing takes place only at temperatures above 600 K [12], one should remark that a fuel oxidation event occurring in-pile at low temperature may lead to more complex oxidation and fission product release conditions than those examined here.

An investigation of the oxidation behaviour in air of samples of irradiated UO_2 was performed in the temperature range 400–670 K (Fig. 3) with a sufficiently large sample (a few grams) so that the weight gain could be measured at time intervals, and XRD analysis was performed to record the progressive modifications of the cubic UO_{2+x} phase and the appearance of orthorhombic U_3O_8. Above 600 K the oxidation kinetics was fast at the beginning, causing O/U → 2.5 within a few hours treatment. The oxygen intake became then slower, O/U

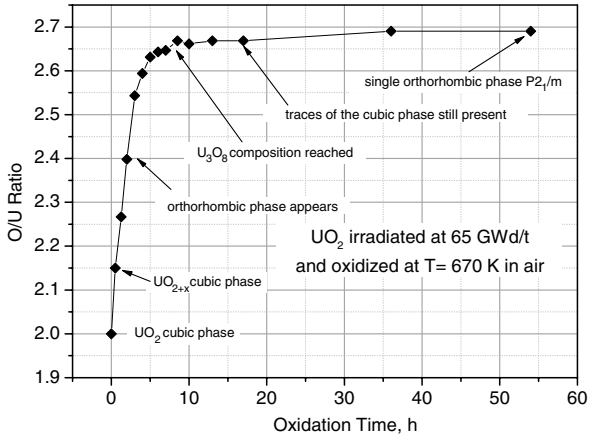

Fig. 3. Oxidation curve of the irradiated sample as a function of time.

reaching the value of 2.66 after 10 h at 670 K – but only after 50 h at 620 K. A further increase of O/U up to 2.7 was measured for annealing times up to 150 h. At lower temperatures, the cubic phase persisted even after 500 h treatment with O/U values just above 2.5, showing a small but constant increase rate.

The XRD patterns indicate complete formation of a U_3O_8 phase only for oxygen stoichiometry slightly higher than that of the octoxide formula, whilst at this composition traces of a cubic phase were always detected. Due to the small practicable size of the samples and the affordable measurement times, only a restricted segment of the XRD

spectrum could be accurately recorded. The peak positions were in agreement with those of the α-phase, however, the signal-to-noise ratio was too low for a precise resolution of the bands of closely spaced reflections characteristic of this structure. Furthermore, there were indications that the observed bands contained a larger number of reflections than those of the orthorhombic α-phase. Based on these observations, the obtained irradiated octoxide was identified as the monoclinic phase found by Chodura and Mal [13]: space group $P2_1/m$, with $\{a,b,c\} = \{1.191, 0.671, 0.827\}$ nm and $\gamma = 89°$. This crystal structure is apparently very close to that of the α-phase (by doubling the c parameter), the angular asymmetry being small. The Roentgen density is effectively the same.

4. Experiment

The irradiated fuel samples were small pieces of about 1 mm^3 volume taken from the periphery of a pellet; however, the external high-burn-up rim was not encompassed in the extracted samples, so that their ceramographic structure after irradiation was similar to the ordinary one.

The fission product fractional vaporisation curves were first measured in non-oxidized samples until complete sublimation. The results, plotted in Figs. 4 and 5, provide information on the different release stages of the fission gas. Analysis of these curves indicates presence of gas on grain boundaries in fractions ranging from 5% to 10% of the inventory.

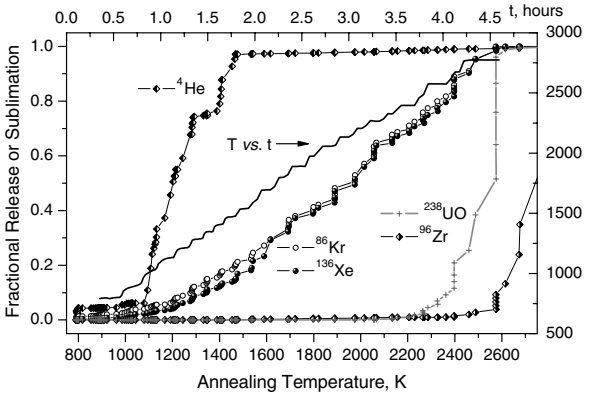

Fig. 4. Fractional release by vaporisation of representative irradiated fuel components under vacuum, starting from end-of-life conditions.

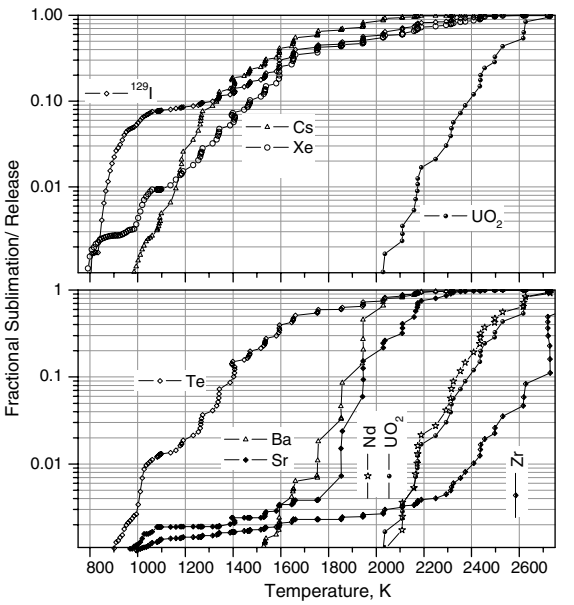

Fig. 5. Logarithmic plot of the fractional release of volatile and less volatile fission products vs. temperature.

4.1. Thermal treatments and oxidation conditions

Three types of experiments have been carried out.

(A) *Vaporisation of non-oxidized reactor-irradiated samples*: they were stepwise annealed in the Knudsen cell (KC) in a vacuum up to 2800 K. Selected nuclides were continuously detected by MS until full sublimation of the sample. Analysis of the UO(g) and UO_3(g) were carried out. The method was based on selective ionization of UO, UO_2 and UO_3 at increasing electron collision energies from the mono- and dioxide ionization potential (~5 eV) upwards. The precision of the calibration is proportional to that of the MS signals of UO^+ and UO_2^+ at low ionization energies (~20%). The concentration of the mono- and dioxide molecules in the vapour indicates that the sample was initially stoichiometric, undergoing, however, significant reduction above 2200 K. The ceramographic structure of the sample at different stages of the annealing programme is shown in Fig. 6. It can be seen that the initial grain size of approximately 5 μm is maintained up to 2400 K, since formation of large intergranular pores prevents diffusion-driven grain growth.

(B) *Oxidation in the KC and subsequent thermal annealing under fixed oxygen pressure*: samples (20 mg) of fuel under end-of-life conditions were

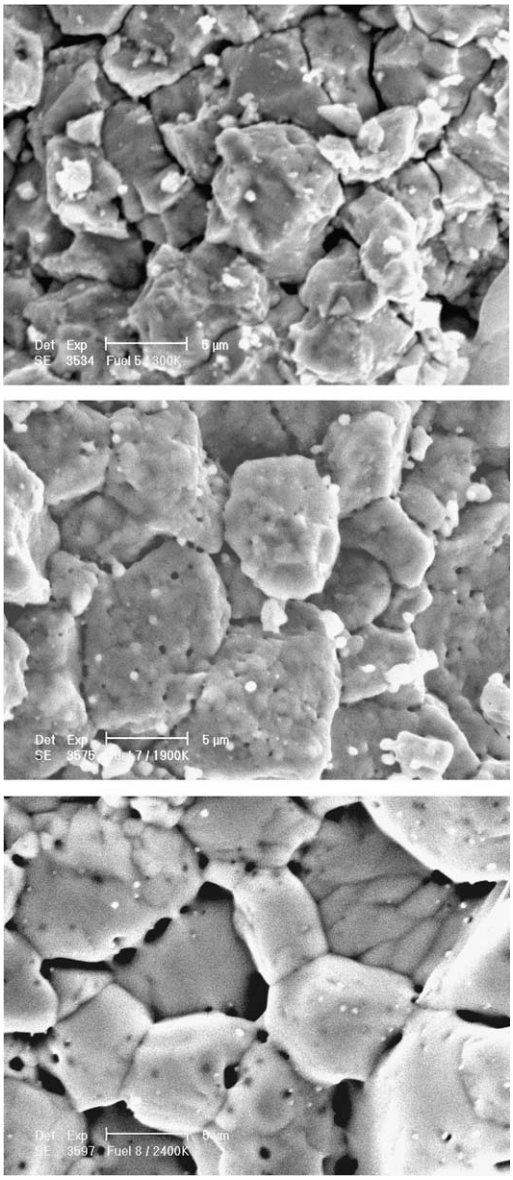

Fig. 6. Micrographs (SEM) of UO_2 fuel under end-of-life (65 GWd t^{-1}) conditions (top) and after treatment in vacuum at 1900 K (middle) and 2400 K (bottom).

annealed at temperatures between 750 K and 850 K in the KC for 4 h under an oxygen partial pressure corresponding to an equilibrium oxygen potential slightly higher than that of U_3O_8, as reported in Ref. [4]. After this oxidation stage, the samples were submitted to a linear heating programme under 1000 Pa oxygen until complete sublimation.

(C) *Oxidation of irradiated samples in a furnace in air and subsequent thermal annealing in the KC:* small fragments (10–20 mg) of previously oxidized samples were subsequently treated in the KC under vacuum up to temperatures at which the measured fractional fission product (FP) release attained significant values without effective changes of the oxide stoichiometry. The composition stability in this temperature range was previously checked [6]. The thermal annealing programme was finally terminated at higher temperatures, where the sample was completely sublimed in a progressively reduced form. This terminal stage had the sole scope to determine for each nuclide the total amount released, and to make it possible to normalise the measured fractional release curves to the initial inventory. In addition, the total amount of krypton and xenon isotopes escaped during these treatments was captured in a cold trap and measured afterwards by mass spectrometry by using a spike method. From the obtained absolute concentrations, we could confirm that the fraction of fission gas escaped during the previous oxidation in air was less than a few percents of the fuel inventory at end-of-life. Fig. 7 shows the porous ceramographic structure of the sample after low-temperature oxidation and after a treatment at 1850 K, where the release process is completed. At this temperature the grains are intersected by 'woodworm channels' and a sub-grain structure is formed, with cells of less than 1 μm size. Actually, we often observed high gas retention in spongy structures consisting of small grains with homogeneously distributed spherical pores (like, for instance, the oxidized fuel, and the high-burn-up rim structure). Percolation patterns and venting of these pores occurs at higher fractional porosities than in customary sintered structures. The results reported in the following sections show that the highly oxidized fuel retained approximately 20% of the fission gas, which escaped at temperatures higher than that of oxidation.

4.2. Gas release in the three experiments

Evaporation of most volatile fission products does not take place according to classical Knudsen mechanisms based on definite equilibrium pressure conditions. Therefore, gas release processes were measured by maximizing the cell aperture to obtain high MS signals. On the other hand, this limited the achievable oxygen pressure in the cell to approximately 1000 Pa, corresponding to the equilibrium partial pressure over U_3O_8 at about 1500 K. Therefore, above this temperature the sample underwent

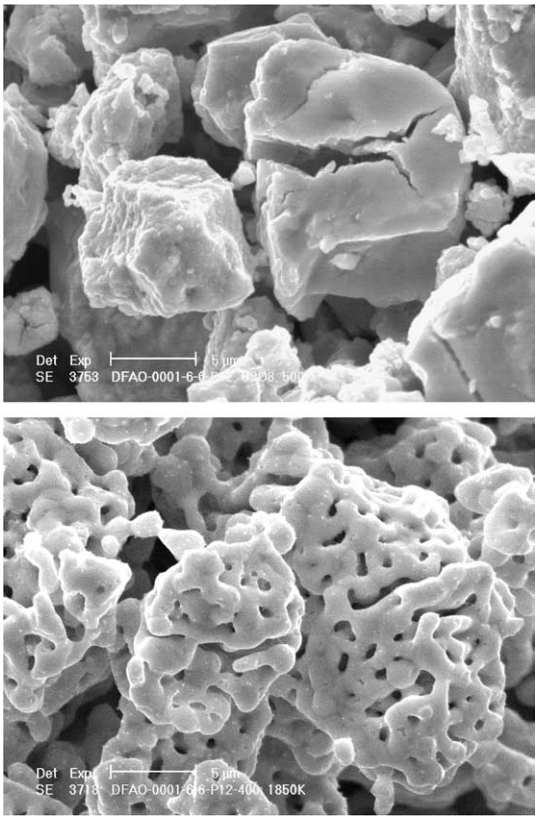

Fig. 7. Micrographs (SEM) of UO_2 at 65 GWd t^{-1} oxidized in air (top) and after annealing under 1000 Pa oxygen at 1850 K.

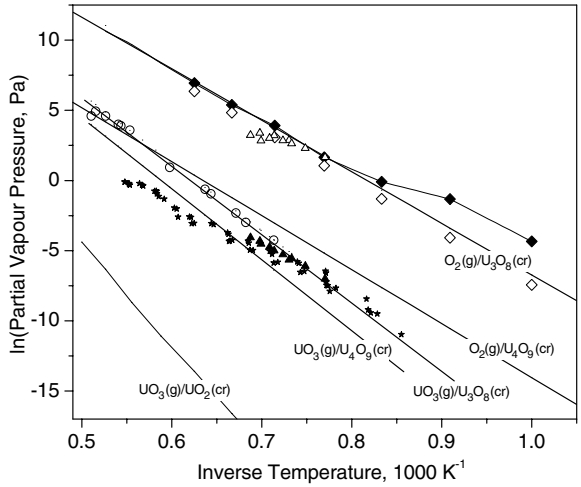

Fig. 8. Behaviour of the vapour components during KC thermal annealing of oxidized fuel. The open symbols represent the vapour pressures of UO_3(g) and O_2 over a reference sample of U_3O_8 measured with a KC aperture of 0.2 mm size. The full symbols represent measurements on irradiated fuel oxidized in air, as in experiment (B). The full lines are the pressures calculated from the IVTAN database [1].

progressive chemical reduction due to non-congruent sublimation. In the graph of Fig. 8 the measured equilibrium partial pressure of UO_3(g) illustrates how the stoichiometry of the sample decreased with increasing temperature. These data are further explained and commented in Ref. [6]. The measured fractional release curves are plotted in Figs. 9–11, and compared with those obtained by vaporising non-oxidized fuel in a vacuum (Figs. 4 and 5).

4.2.1. (Case A): Release in a vacuum from non-oxidized samples

Fission-product vaporisation from irradiated UO_2 under end-of-life conditions was previously investigated in an extended experimental programme involving different fuel types in the burn-up range up to 100 GWd t^{-1}. In this context, the results plotted in Figs. 4 and 5 are typical for a fuel of 65 GWd t^{-1} burn-up, irradiated at temperatures below 800 K. The graph of Fig. 4 gives us an idea about the temperature interval in which effective release or vaporisation of the various fuel components occurs, from the fastest (helium) to one of the least volatile phases (e.g., ZrO_2). This temperature interval extends from approximately 1000 K to 2800 K. The plotted UO(g) curve describes the uranium oxide vapour species which is detected to the last during the ultimate sublimation stage of the dioxide, which under high vacuum is reduced below the congruent vaporisation composition. The release/vaporisation behaviour of the sample can be summarised as follows:

- Iodine, ^{129}I(g), is the first FP to be detected above 800 K in comparatively large fractional amounts, but its initial release stage terminates at approximately 1000 K. Above 1300–1400 K caesium becomes the predominant vapour species and is the first to reach total release at approximately 1800 K.
- Release of xenon starts also at 800 K, but it augments less with temperature and its fractional value remains below that of ^{129}I and of all Cs isotopes. Kr is slightly faster released than Xe, but the difference is sometimes within the experimental error.
- Tellurium (^{130}Te) release is similar to that of all Cs isotopes. Above 1000 K its volatility in both the elementary and oxide form is sufficiently high

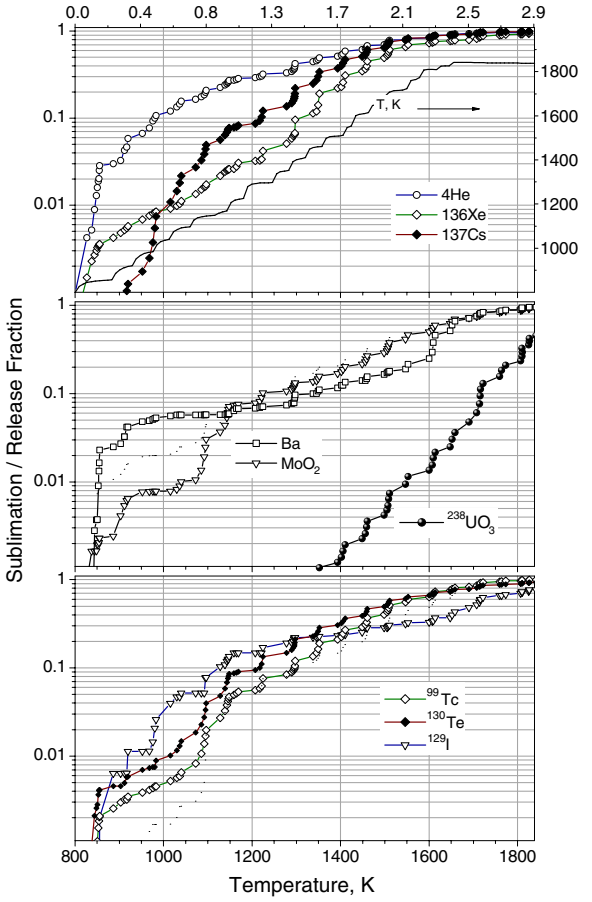

Fig. 9. Release by vaporisation processes from oxidized irradiated fuel in experiment (B).

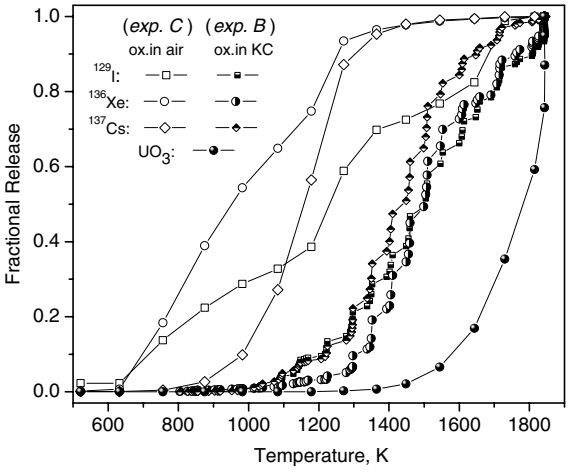

Fig. 10. Comparison of volatile fission product release in experiments (B) and (C).

to produce instant vaporisation when Te reaches a free surface.

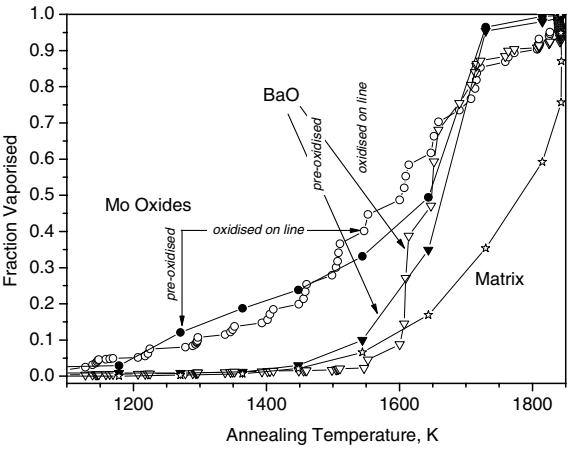

Fig. 11. Less volatile fission-product vaporisation in experiments (B) and (C).

- The strontium and barium curves are similarly displaced towards higher temperatures; substantial release starts above 1800 K.
- Rare Earth oxide vaporisation rate approximately coincides with that of the dioxide matrix.
- The fission-gas release curve as a function of temperature is almost symmetrically intermediate between that of helium and the least volatile components.
- After total UO_2 sublimation, in the KC it remains only ZrO_2, which completely vaporises at 2800 K, and some metallic fission products (Mo, Ru, Pd, Rh), which at 2500 K are less volatile than UO_2.

4.2.2. (Case B): Release in samples after oxidation to U_3O_8 in the KC under controlled atmosphere

The samples were oxidized under controlled conditions at 750 K during 4 h. Negligible release was detected by MS during this stage. In the following annealing programme, release/vaporisation curves indicate higher in-solid mobilities in the oxidized than in the non-oxidized samples. Furthermore, some relevant changes in the vaporisation sequence of the various components were observed:

- For fission gas and very volatile fission products, the onset temperature of release (Fig. 9) is only slightly lower than in case (A). The negative shift, however, increases to approximately 200 K during the bulk release stage. Remarkably, the relative trend of the Cs- and Xe-release curves remains the same as in case (A), with fractional release starting later for Cs (around 960 K vs.

800 K), but increasing faster and exceeding that of Xe above 1000 K.
- The release of helium in the oxidized sample is not much faster than in the non-oxidized fuel, terminating at temperatures above 1600 K, where U_3O_8 was progressively reduced to cubic UO_{2+x}.
- Molybdenum and technetium appear in the vapour in the form of oxides. About 1% is released below 1000 K in a well separated stage. The mass is released between 1200 K and 1800 K. Barium exhibits a similar behaviour.
- Lanthanides are absent in the vapour, and their oxide gaseous species appear only at temperatures where U_3O_8 is completely vaporised, indicating that they are not affected by over oxidation of fuel UO_2.

4.2.3. (Case C): Release in samples after oxidation to U_3O_8 in air

The results of release from the α'-U_3O_8 phase are plotted in Figs. 10 and 11, where one can see that:

- Release of fission gas and volatile fission products is markedly faster with a shift of the fractional release curves from 200 K to 400 K towards lower temperatures. The enhancement is larger for xenon than for iodine and caesium.
- The less volatile fission products behave similarly in the two phases oxidized in air and in the KC.

5. Analysis of the gas release stages

Analysis of the measured release curves is presently affordable for inert gases, where simpler diffusion processes are involved. The gas is effectively insoluble in the matrix and its migration or precipitation in bubbles is only governed by the Brownian motion of the diffusing species and/or by the matrix self-diffusion. No phenomenological forces are supposed to be active, the diffusion flux being merely given by Fick's law in conjunction with the assumed zero concentration at the external and internal free surfaces. Generally, the measured fractional release curves $R = R(T,t)$ cannot be fitted by a simple model of diffusion in a finite, homogeneous medium. On the other hand, the observed good reproducibility of the main features let us infer that the ruling mechanisms, although difficult to quantify from the atomistic point of view, are somewhat simple.

5.1. Assumed diffusion equations

Numerous similar applications have shown that assumption of three diffusion stages is in most cases sufficient to reproduce the observations: apparently, after an initial fast-release stage, the gas first diffuses to free surfaces and sinks, and from these it follows preferential patterns to reach the free surface. In principle, to fit the experimental data we do not need to specify a priori the nature of the sinks and the morphology of the release patterns, although we might conjecture them. The method of analysis can be the same as that previously adopted for fission gas and helium in non-oxidized fuels [14,15]. Briefly, the diffusing gas is assumed to be possibly distributed in three states, with concentrations respectively pertaining to an initial location on grain boundaries (c_1), in the grain volume (c_2) and in, a priori non-specified, tapping sites (c_3) from which it can further escape with a different mobility. The ruling rate equations of the normalised fractional concentrations are assumed to have the form:

$$\begin{aligned}
&\frac{dc_1}{dt} = -H_1 c_1,\\
&\frac{dc_2}{dt} = -H_2 c_2 - K_2 c_2,\\
&\frac{dc_3}{dt} = K_2 c_2 - H_3 c_3,\\
&R = 1 - c_1 - c_2 - c_3;\\
&c_1 = c_{1,0}; \quad c_2 = c_{2,0}; \quad c_3 = c_{3,0} \quad \text{at } t = t_0,
\end{aligned} \tag{1}$$

where R represents the fraction released. The sketch of Fig. 12 visualises the meaning of the terms in Eq. (1).

The reaction-rate constant, K_2, is expressed as the product of a diffusion coefficient, $D_2 = D_{2,0}\exp(-\Delta H_2/kT)$, times a sink-strength constant k_s^2:

$$k_s = (K_2/D_2)^{1/2}. \tag{2}$$

To obtain k_s one needs the full expression of the diffusion coefficient, including the pre-exponential factor. Since the precision of this latter, as obtained by numerical fitting, is low, $D_{2,0}$ was assessed by averaging the best fitting results on different curves. It should be noted that $D_{2,0}$ appears in the analysis only through the following Eq. (3), where one can see that its influence on the correlation between K_2 and H_2 is rather week.

The relationship between $H_{2,0}$ and $K_{2,0}$ as defined by the assumed concomitant release rate from a

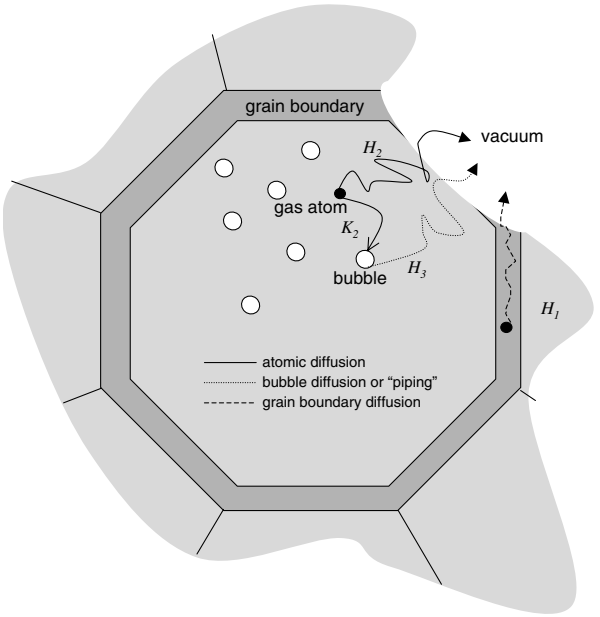

Fig. 12. Schematics of the diffusion processes formulated in Eq. (1). The mathematical formalism does not require any a priori definition of the operating diffusion mechanisms, the only assumption being their single-energy thermal activation. These can be, for instance, a primary mechanism (1) based on atomic gas volume diffusion, the flux of which is split between desorption and precipitation in traps (bubbles); of a secondary mechanism (2) involving bubble migration or 'piping', i.e., migration along preferential patterns (dislocations); and a third mechanism consisting in fast diffusion of gas previously migrated to grain boundary. Each mechanism has an individual thermal activation enthalpy and an (entropic) pre-exponential factor depending on the size and morphology of the diffusion domain and on the 'basic jump' frequency of the diffusing species.

spherical grain of size a (with coefficient H_2) and the capture rate by sinks (with coefficient K_2) has the expression [16]:

$$H_2 = \frac{3K_2}{1-3G}; \quad G = -\frac{1}{a^2k_s^2} + \frac{\coth(ak_s)}{ak_s} \tag{3}$$

The other coefficients of the reaction rate equations are written as: $H_j = H_{j,0}\exp(-\Delta H_j/kT)$, where the frequency $H_{j,0}$ is the ratio of the pre-exponential constant of the ruling diffusion coefficient, D_j, and the square of an effective dimension of the diffusion domain. However, as long as a reaction is not correlated with others, it is not necessary to provide this expression of $H_{j,0}$. This is obviously meant for purposes of numerical analysis, where one strives for information on the ruling activation energies of diffusion. A physical interpretation should be further pursued. For instance, the gas diffusion mechanisms examined here are certainly associated with porosity growth and venting, and the significance of the effective activation energy may not be related to gas mobility only – as, for instance, in experiment (A), where the third stage doubtless corresponds to release of gas in bubbles by matrix sublimation. However, as long as a thermally activated process is governing matter transport, the coefficients $H_{j,0}$ may be qualitatively interpreted as the product of the typical frequency of the elemental 'jumps' times the square of the consequent fractional displacement of the gas over the size of the diffusion domain. In some sense, the phenomenological coefficients have a far-reaching significance that may help us in devising more detailed models.

For a constant temperature and given initial values of the variables, equation system (1) has the simple general integral:

$$\begin{aligned} c_1 &= c_{1,0}e^{-H_1 t}, \\ c_2 &= c_{2,0}e^{-(H_2+K_2)t}, \\ c_3 &= e^{-H_3 t}\left[c_{3,0} + \frac{c_{2,0}K_2}{H_2-H_3+K_2} - \frac{c_{2,0}K_2 e^{(H_3-H_2-K_2)t}}{H_2-H_3+K_2}\right] \end{aligned} \tag{4}$$

that can be applied to any arbitrary sequence of temperature steps, where the exponential T-dependence of the coefficients H and K is expressed through their respective activation energies.

Thus, the resulting expression of $R(T)$ was used to fit the experimental curves with a computer programme where a numerical calculation strategy is devised to obtain the most robust solutions. The results are collected in Table 1 for xenon and helium.

5.2. Fitting results (Table 1)

For experiment (B), where the irradiated sample was initially oxidized in the KC to α-U_3O_8, only ≈2% of the xenon appears to be early released starting from grain boundary positions (first stage, $\Delta H_1 = 0.75$ eV). The central second stage, with activation energy $\Delta H_2 = 2.07$ eV, is split between direct migration of gas to the open surfaces (63%) and an intermediate precipitation into sinks (35%) from which it finally escapes with an activation energy of 0.9 eV (third stage). The activation energy of the second stage is clearly lower than that of 3.25 eV measured in the non-oxidized sample in experiment (A). This latter is in agreement with previous measurements in irradiated UO_2 [17], which indicate a progressive decrease of the fission-gas

Table 1
Fitted parameters of Eq. (1)

	Activation energy/k, K	Time constant, s^{-1}	Yield	Mechanism
Diffusion of xenon (^{136}Xe, ^{134}Xe)				
Experiment (A): UO_2	$\Delta H_1 = 35190$	$H_{1,0} = 5.2 \times 10^5$	0.20	g.b. diffusion
	$\Delta H_2 = 37650 \pm 100$	$H_{2,0} = (6.0 \pm 0.05) \times 10^4$	0.56	Volume diffusion
		$K_{2,0} = (2.58 \pm 0.05) \times 10^4$	0.24	Precipitation
	$\Delta H_3 = 70450 \pm 200$	$H_{3,0} = (8.9 \pm 40) \times 10^{10}$	0.24	Vaporisation
Experiment (B): α-U_3O_8	$\Delta H_1 = 8700$	$H_{1,0} = 5.12$	0.02	g.b. diffusion
	$\Delta H_2 = 23170 \pm 240$	$H_{2,0} = (6.0 \pm 0.3) \times 10^3$	0.63	Volume diffusion
		$K_{2,0} = (3.5 \pm 0.5) \times 10^3$	0.35	Precipitation
	$\Delta H_3 = 11540 \pm 2000$	$H_{3,0} = (6.6 \pm 40) \times 10^{-1}$	0.35	Sub-g.b. diffusion
Experiment (C): α′-U_3O_8	$\Delta H_1 = 13320$	$H_{1,0} = 1.8 \times 10^5$	0.2	g.b. diffusion
	$\Delta H_2 = 14000 \pm 100$	$H_{2,0} = (6.0 \pm 0.3) \times 10^3$	0.27	Volume diffusion
		$K_{2,0} = (1.1 \pm 0.2) \times 10^4$	0.53	Precipitation
	$\Delta H_3 = 8580 \pm 850$	$H_{3,0} = 2.3 \pm 19$	0.53	Sub-g.b. diffusion
Diffusion of helium (^4He)				
Experiment (B): α-U_3O_8	$\Delta H_1 = 17350$	$H_{1,0} = 2.33 \times 10^5$	0.10	g.b. diffusion
	$\Delta H_2 = 18420 \pm 300$	$H_{2,0} = (6.00 \pm 0.1) \times 10^3$	0.11	Volume diffusion
		$K_{3,0} = (4.55 \pm 0.2) \times 10^3$	0.79	Precipitation
	$\Delta H_3 = 10150 \pm 300$	$H_{3,0} = 0.63 \pm 1.32$	0.79	Sub-g.b. diffusion
Experiment (C): α′-U_3O_8	$\Delta H_1 = 5365$	$H_{1,0} = 8.64 \times 10^3$	0.4	g.b. diffusion
	$\Delta H_2 = 7947 \pm 120$	$H_{2,0} = (6.00 \pm 0.1) \times 10^3$	0.14	Volume diffusion
		$K_{3,0} = (2.03 \pm 0.2) \times 10^4$	0.46	Precipitation
	$\Delta H_3 = 2500 \pm 280$	$H_{3,0} = (3.8 \pm 7) \times 10^{-3}$	0.46	Sub-g.b. diffusion

n.b.: The errors represent the correlated fitting stabilities. For the first stage the error is not given since this quantity is obtained independently of the second and third stage.

diffusion enthalpy with burn-up. The results of the analysis for ^{136}Xe are shown in Fig. 13.

In experiment (C), where the oxidation state corresponds to the less dense α′-U_3O_8 crystal phase, ≈20% of the gas is released from initial grain boundary positions ($\Delta H_1 = 1.1$ eV), whilst 27% reaches the free surface in the second stage ($\Delta H_2 = 1.27$ eV) and 53% is first trapped and then released with a low energy activation ($\Delta H_3 = 0.74$ eV).

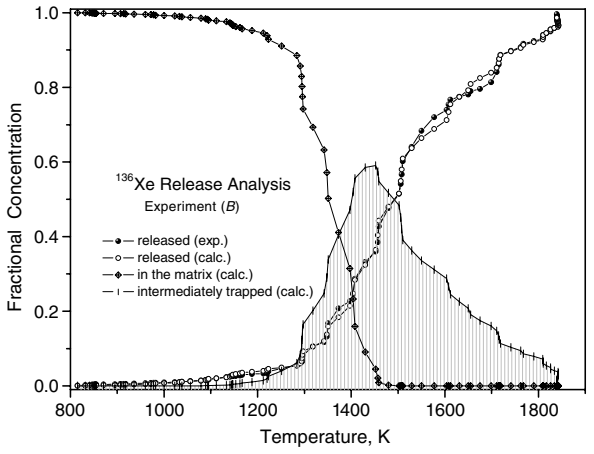

Fig. 13. Typical analysis of a xenon release curve in experiment (B), based on the integral of Eq. (1).

These results were obtained from a sufficiently robust numerical fitting; however the interpretation of the parameters is still conjectural. In our case, the instability of the crystal and of the sintered structure makes the analysis more complicated. Actually, the results of rare gas diffusion measurements in U_3O_8 published in the literature show a great scatter that can be only explained by a shortcoming in the raw data analysis. For instance, from repeated measurements in reactor irradiated U_3O_8 Lindner and Matzke [18] found a Xe-diffusion enthalpy ranging from 0.75 eV to 1.1 eV, with, however, uncommonly low pre-exponential factors (10^{-14}–10^{-15} $m^2\,s^{-1}$). However, values closer to ours were obtained by Kennett and Thode (1.74 eV) [19] from fission product extraction experiments. In this regard, one should consider that in the former experiments the lattice was highly damaged, whilst in the latter the sample was treated similarly to ours. Furthermore, it is worth remarking that in subsequent experiments

with ion-implanted gas, Matzke measured a diffusion activation energy of ^{222}Rn in undamaged U_3O_8 of 3.8 eV [20] that is larger than that obtained in our experiment (B), and is hardly compatible with his previous results on xenon.

The data reported in Table 1 are certainly reliable in the given interpretation context. However, by applying these data to other cases, the relevance of possible variations of the frequencies $H_{i,0}$ must be considered. These depend not only on the atomic relaxation time of the diffusing species, but also on dimensionless structural parameters that can be expressed in terms of grain and sub-grain size, dislocation density and porosity distribution. In Figs. 14 and 15 are respectively shown, the Arrhenius plots

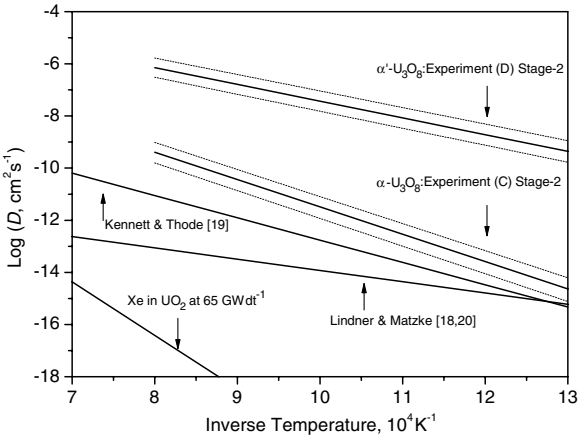

Fig. 14. Xenon diffusion coefficient in α- and α′-U_3O_8 in the second stage. The lines are plotted in the experimental temperature interval in which the sample composition could be kept constant.

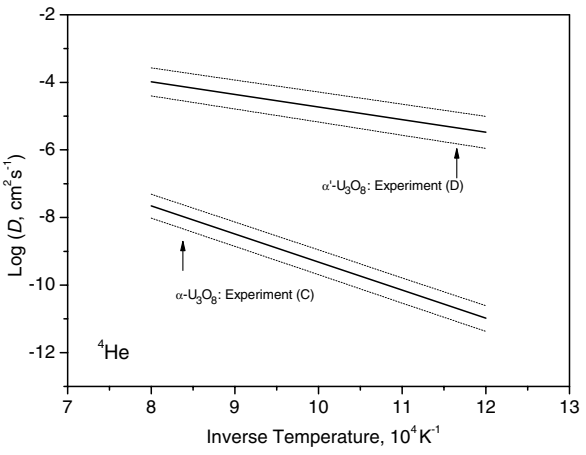

Fig. 15. Idem as in Fig. 14, for helium.

of the measured xenon and helium diffusion coefficients in the second stage that likely corresponds to atomic diffusion of gas. The dashed lines represent the probable error including an uncertainty of a factor of two in the effective grain size. The error affects mainly $D_{2,0}$ and only marginally the activation energy. The values of $D_{2,0}$ averaged over different experiments are in the range 10^{-4}–10^{-5} $m^2\,s^{-1}$ (see Fig. 14).

The release curves for helium could be precisely analysed for experiment (B), whilst the data obtained in experiment (C) are less reproducible. In the former experiment, however, one can note that in the second stage (volume-diffusion) the activation energy is 1.6 eV, and those of first and third stage are similarly low (1.49 eV and 0.87 eV, respectively). In experiment (C) the diffusion energies are markedly lower, with 0.7 eV for the second stage and a few tens of eV for the first and third stage.

One should finally point out that general applications of these results for gas release prediction are possible if the integral of Eq. (1) is used, and the above mentioned rate coefficients are representative for the given conditions. For the case of U_3O_8, where release is completed before the matrix sublimation stage, the coefficients of Table 1 can be reasonably applied to describe in-pile events.

6. Conclusions

Samples of a BWR fuel rod irradiated up to 65 GWd t^{-1} were oxidized in laboratory at low temperature up to formation of U_3O_8. Vaporisation and release phenomena were investigated in a Knudsen cell with on-line mass spectrometer.

Oxidation conspicuously increases atomic mobilities of volatile species dissolved in the matrix, including molybdenum oxides. Lanthanides oxides, however, remain in the solid phase even after complete sublimation of U_3O_8.

Analysis of the fission-gas and helium release curves was carried out under defined starting conditions with large concentrations of gas homogeneously dispersed in the matrix. Under thermal annealing conditions with increasing temperature programmes, release was observed to occur in three subsequent stages. In the first one, gas is released starting from grain boundary positions; in the second stage, volume diffusion takes place leading in part to release and in part to trapping on sites from which release is further taking place with different activation energy (third stage). Only the

second stage can be identified as an atomic diffusion process in a perfect U_3O_8 lattice, whilst the third stage is probably associated to a development of sub-microscopic cells on the interface of which gas migrates with low activation energies.

In practice, use of diffusion data to predict gas release in oxidized fuel is not straightforward, since it requires a sufficiently accurate formulation of the three stages, for instance, as summarised in the analytical part of the paper.

Acknowledgements

This work was performed under the priority action 'Safety of Nuclear Fuel', as part of the 6th Framework Programme of the European Commission. The authors would like to gratefully acknowledge the valuable analysis work of P. Boulet for XRD and H. Thiele for electron microscopy.

References

[1] L.V. Gurvich, V.S. Iorish, D.V. Chekhovskioi, V.S. Yungman, NIST Special Database 5, IVTANTHERMO, CRC, Boca Raton, FL, 1993.
[2] P.-Y. Chevalier, E. Fischer, B. Cheynet, J. Nucl. Mater. 303 (2002) 1.
[3] C. Guéneau, M. Baichi, D. Labroche, C. Chatillon, B. Sundman, J. Nucl. Mater. 304 (2002) 161.
[4] D. Labroche, O. Dugne, C. Chatillon, J. Nucl. Mater. 312 (2002) 21.
[5] D. Manara, M. Sheindlin, C. Ronchi, J. Nucl. Mater. 342 (2005) 148.
[6] J.-P. Hiernaut, J.-Y. Colle, R. Pflieger-Cuvellier, J. Jonnet, J. Somers, C. Ronchi, J. Nucl. Mater. 344 (2005) 246.
[7] B.O. Loopstra, Acta Crystallogr. B 26 (1970) 651.
[8] A.F. Andresen, Acta Crystallogr. B 11 (1958) 612.
[9] R.M. Herak, J. Inorg. Nucl. Chem. 32 (1970) 3793.
[10] R.M. Berman, M.L. Bleiberg, W. Yeniscavich, J. Nucl. Mater. 2 (1960) 129.
[11] B.G. Childs, J. McGurns, Report CR-Met. 868, 1959.
[12] E.R. Boyko, J.D. Eichenberg, R.B. Roof, E.K. Halteman, Bettis Techn. Rev. WAPD-BT-6, 1958, p. 64.
[13] B. Chodura, J. Mal, in: Proceedings of the 2nd United Nations International Conference on Peaceful Uses of Atomic Energy, Geneva, vol. 28, 1958, p. 223.
[14] F. Capone, J.P. Hiernaut, M. Martellenghi, C. Ronchi, Nucl. Sci. Eng. 124 (1996) 436.
[15] C. Ronchi, J.P. Hiernaut, J. Nucl. Mater. 325 (2004) 1.
[16] C. Ronchi, J. Sakellaridis, C. Syros, Nucl. Sci. Eng. 95 (1987) 282.
[17] J.P. Hiernaut, C. Ronchi, J. Nucl. Mater. 294 (2001) 39.
[18] R. Lindner, Hj. Matzke, Atomkernenergie 9 (1964) H.1/2.
[19] T.J. Kennett, H.G. Thode, Can. J. Phys. 38 (1960) 945.
[20] H. Matzke, J. Mater. Sci. 2 (1967) 444.